A&A, 686, A33 (2024)
https://doi.org/10.1051/0004-6361/202347912

Astronomy & Astrophysics

Imaging detection of the inner dust belt and the four exoplanets in the HR 8799 system with JWST's MIRI coronagraph⋆

Anthony Boccaletti[1], Mathilde Mâlin[1], Pierre Baudoz[1], Pascal Tremblin[2], Clément Perrot[1], Daniel Rouan[1], Pierre-Olivier Lagage[2], Niall Whiteford[4], Paul Mollière[3], Rens Waters[5,6,7], Thomas Henning[3], Leen Decin[10], Manuel Güdel[8,3,9], Bart Vandenbussche[10], Olivier Absil[11], Ioannis Argyriou[10], Jeroen Bouwman[3], Christophe Cossou[2], Alain Coulais[2,13], René Gastaud[12], Alistair Glasse[14], Adrian M. Glauser[9], Inga Kamp[15], Sarah Kendrew[16], Oliver Krause[3], Fred Lahuis[7], Michael Mueller[15], Goran Olofsson[17], Polychronis Patapis[9], John Pye[18], Pierre Royer[10], Eugene Serabyn[23], Silvia Scheithauer[3], Luis Colina[19], Ewine F. van Dishoeck[20], Göran Ostlin[21], Tom P. Ray[22], and Gillian Wright[14]

(Affiliations can be found after the references)

Received 8 September 2023 / Accepted 27 February 2024

ABSTRACT

Context. The MIRI instrument on board JWST is now offering high-contrast imaging capacity at mid-IR wavelengths, thereby opening a completely new field of investigation for characterizing young exoplanetary systems.
Aims. The multiplanet system HR 8799 is the first target observed with MIRI's coronagraph as part of the MIRI-EC Guaranteed Time Observations (GTO) exoplanet program, launched in November 2022. We obtained deep observations in three coronagraphic filters, from ∼10 to 15 µm (F1065C, F1140C, F1550C), and one standard imaging filter at ∼20 µm ($F2100W$). The goal of this work is to extract photometry for the four planets and to detect and investigate the distribution of circumstellar dust.
Methods. Using dedicated observations of a reference star, we tested several algorithms to subtract the stellar diffraction pattern, while preserving the fluxes of planets, which can be significantly affected by over-subtraction. To obtain correct measurements of the planet's flux values, the attenuation by the coronagraphs as a function of their position must be accounted for, as well as an estimation of the normalisation with respect to the central star. We tested several procedures to derive averaged photometric values and error bars.
Results. These observations have enabled us to obtain two main results. First, the four planets in the system are well recovered and we were able to compare their mid-IR fluxes, combined with near-IR flux values from the literature, to two exoplanet atmosphere models: `ATMO` and `Exo-REM`. As a main outcome, the MIRI photometric data points imply larger radii (1.04 or 1.17 R_J for planet b) and cooler temperatures (950 or 1000 K for planet b), especially for planet b, in better agreement with evolutionary models. Second, these JWST/MIRI coronagraphic data also deliver the first spatially resolved detection of the inner warm debris disk, the radius of which is constrained to about 15 au, with flux densities that are comparable to (but lower than) former unresolved spectroscopic measurements with Spitzer.
Conclusions. The coronagraphs coming from MIRI ushers in a new vision of known exoplanetary systems that differs significantly from shorter wavelength, high-contrast images delivered by extreme adaptive optics from the ground. Inner dust belts and background galaxies become dominant at some mid-IR wavelengths, potentially causing confusion in detecting exoplanets. Future observing strategies and data reductions ought to take such features into account.

Key words. techniques: high angular resolution – techniques: image processing – planets and satellites: detection – stars: individual: HR 8799

1. Introduction

Massive giant planets in large orbits (>5 au) are found to be relatively rare, as inferred from direct imaging surveys (Vigan et al. 2020; Nielsen et al. 2019) and even statistics from radial velocity surveys are not complete in such cases (Lagrange et al. 2023). Therefore, every single detection is significant when it comes to improving our understanding of how such massive planets can form in the outer parts of planetary systems and how they can impact the fate of other planets. Historically, young giant planets have been discovered and characterized in the near-IR with general facilities, or dedicated high-contrast instruments on the ground. However, little is known about their properties at longer wavelengths. Observations from the ground at mid-IR have proven to be difficult because of sensitivity issues and essentially yield no clear detections (Wagner et al. 2021; Skaf et al. 2023). The *James Webb* Space Telescope (JWST) mission (Gardner et al. 2023) is definitely a game-changer in this field by providing high angular resolution together with high-contrast capacities at wavelengths longer than ∼5 µm, which had not even been accessible in the past. In this respect, mid-IR is crucial with respect to setting independent constraints on the luminosity, temperature, and radius measurements of planets, as well as to provide access to molecules such as ammonia. Carter et al. (2023) presented JWST observations of a giant planet, previously discovered with SPHERE at the VLT (Chauvin et al. 2017), and observed for the very first time at 10 and 15 µm with the JWST Mid-Infrared Instrument (MIRI, Wright et al. 2015) and its coronagraphic system (Boccaletti et al. 2015).

⋆ Data for Fig. 1 are available at the CDS via anonymous ftp to `cdsarc.cds.unistra.fr` (`130.79.128.5`) or via `https://cdsarc.cds.unistra.fr/viz-bin/cat/J/A+A/686/A33`

Since its discovery in 2008 at Keck (Marois et al. 2008, 2010), the HR 8799 multiplanet system has been the focus of numerous studies to explore the atmospheric properties and dynamics as well as the dust content of its debris disk. This system, consisting of four giant planets with masses ranging roughly between 5 and 10 M_J, according to hot-start evolutionary models, and orbital distances of 15.7, 25.7, 39.5, and 68.6 au (Thompson et al. 2023), is often seen as an "upscale" version of a young Solar System (Faramaz et al. 2021). This multiplicity, along with the presence of planetesimal belts make the HR 8799 system unique among all known exoplanetary systems, as it offers a testbed for understanding the formation of planets around early-type stars.

With the objective to characterize the atmospheres of these four planets, spectral analyses have been performed for a broad range of near-IR wavelengths from the z to M bands, in photometry (Currie et al. 2011; Skemer et al. 2014), at low spectral resolution (Bonnefoy et al. 2016; Ingraham et al. 2014; GRAVITY Collaboration 2019), and even with medium-to-high resolution (Barman et al. 2011; Konopacky et al. 2013; Ruffio et al. 2021; Wang et al. 2022). Their colors indicate that these four giant planets differ from field brown dwarfs with notably redder colors, near the L/T transition, which require patchy optically thick clouds and non-equilibrium chemistry to match the observations. Their temperature range from 900 K to 1300 K, with planet b being significantly cooler and fainter, while their surface gravity ranges between $\log(g) = 3.5$ and 4.5 (Bonnefoy et al. 2016). These near-IR data suggest a tendency towards super-solar metallicity. While atmospheric models reproduce rather well the near-IR photometry and spectrum for planets d and e, they are much less effective in fitting planets b and c (Bonnefoy et al. 2016). One issue has been the determination of planet radii which are found to be too small, in particular for planet b with values as small as 0.5–0.7 R_J. For an assumed age of about 30 Myr, evolutionary models have predicted a radius measurement even as large as 1.3 R_J.

At least two molecules have been clearly identified in the atmosphere of the four planets, namely, H_2O and CO, even at low spectral resolution. However there is an ongoing debate about the detection of methane, which is not reproducible from one data reduction to the other (Barman et al. 2015; Petit Dit De La Roche et al. 2018). This is one main difference with field brown dwarfs, the spectra of which show the signature of methane at temperatures cooler than ~1300 K. In addition, the measurement of the C/O ratio is claimed as one of the most promising ways to constrain the formation history (Öberg et al. 2011) and to disentangle between accretion-like and stellar-like mechanisms, the former scenario predicting super-solar values. As of today, there is no clear consensus on the C/O ratio since various studies yield solar or marginally super-solar values (Mollière et al. 2020; Konopacky et al. 2013; Ruffio et al. 2021). Some of the atmospheric properties are well explained by self-consistent atmospheric models such as `Exo-REM` (Charnay et al. 2018). In particular, the colors with respect to the L/T transition can be explained by low gravity planets with clouds, although there is an alternative interpretation with cloudless models that involves fingering convection (Tremblin et al. 2016). Charnay et al. (2018) also explained how low gravity and clouds contribute to reducing the abundance of methane.

The HR 8799 multiplanet system also contains planetesimal belts that are replenishing the system with small dust particles in a collisional cascade. The dust architecture has been essentially inferred from Spitzer spectroscopy (Chen et al. 2006), and IR excess analysis, from which Su et al. (2009) derived the presence of three components: an inner warm (~150 K) belt located at ~6–15 au, an outer cold (~45 K) belt at ~90–300 au, and a halo further out. So far, only the outer cold belt has been spatially resolved at sub-millimeter and millimeter wavelengths (Hughes et al. 2011; Booth et al. 2016; Faramaz et al. 2021). In this picture, the outer edge of the inner belt (and the inner edge of the outer belt) would be sculpted by planet e and b, respectively. However, the size of the disk is not fully in agreement with the analysis of the IR excess which raises some debate about the presence of a fifth planet (Faramaz et al. 2021).

As of today, the HR 8799 multiplanet system has been observed extensively in the near-IR and far-IR regimes, which are complementary and relevant for investigating different physical processes, but was lacking any deep exploration in the mid-IR (Petit Dit De La Roche et al. 2020), which is interesting in the context of planet formation. As to atmosphere characterisation, mid-IR observations at wavelengths longer than 5 μm are valuable to provide more direct measurements of the effective temperature and radius of giant planets with less degeneracies caused by clouds, as well as to discriminate between various atmosphere models. Mid-IR observations encompass the signature of ammonia which has some advantage over methane to provide temperature estimates at least for $T < 1000$ K (Danielski et al. 2018). Moreover, the broad signature of silicate particles can constrain the composition of clouds if present (Miles et al. 2023). Additionally, this spectral range matches the peak of the emission of planets cooler than those with a peak flux in the near-IR, providing the means to push detections to lower masses. Finally, the mid-IR has the ability to probe the intermediate-size grain population (a few to tens of μm), which can be distributed differently than sub-micron sized grains, seen in scattered light, and the larger millimeter-sized grains.

In this paper, we present the first spatially resolved detection of the four planets in the HR 8799 system and of the inner warm disk, in the mid-infrared, with JWST/MIRI. Section 2 describes the observations and the data reduction. In Sect. 3, we detail the photometric measurements used to perform the atmospheric modeling, which we describe in Sect. 4. The detection of the inner disk is addressed in Sect. 5. Finally, the nature of a background object is discussed in Sect. 6 and we conclude in Sect. 7.

2. Observations and data reduction

2.1. Observations

HR 8799 was observed in two runs on November 7, 2022 (filters F1065C and $F2100W$) and November 8, 2022 (filters F1140C and F1550C), under the Guaranteed Time Observations (GTO) program 1194, using both MIRI's Four Quadrant Phase Mask (4QPM) coronagraphs and standard imaging. This source is included in MIRIco, an EU and US coordinated observing effort that makes use of MIRI coronagraphs throughout programs 1194, 1277, and 1241. The log of observations is provided in Table 1. For each coronagraphic filter, we observed back-to-back the target and its associated background (in two dithers) and then the reference star together with its own background. Background images are necessary to remove the "glowstick" effect, as explained in Boccaletti et al. (2022) and are obtained near the target (typically a few tens of arcseconds away). On the contrary, no background observation is necessary for non-coronagraphic imaging data since the star is dithered in four positions across the field of view. While coronagraphic sequences can be obtained at two roll angles, we did not use this capability, which for MIRI is not much relevant given the limited amount of roll (14° at max) combined to a poor angular resolution.

Table 1. Log of observations.

Date/time in UT (month/day/year)	Seq.	Filter	Object	Type	Obs id	N_{group}	N_{int}	N_{dither}	T_{exp} per dither (s)
11/07/2022 21:19	1	F1065C	HR 8799	TARG	obs 7	500	9	1	1080.48
11/07/2022 22:43	3	F1065C	–	BGD	obs 13	500	9	2	1080.48
11/07/2022 23:49	4	F1065C	HD 218261	REF	obs 14	500	2	9	239.92
11/08/2022 01:42	6	F1065C	–	BGD	obs 20	500	2	2	239.92
11/08/2022 08:24	7	F1140C	HR 8799	TARG	obs 8	500	9	1	1080.48
11/08/2022 13:25	10	F1140C	–	BGD	obs 12	500	9	2	1080.48
11/08/2022 14:27	11	F1140C	HD 218261	REF	obs 15	500	2	9	239.92
11/08/2022 16:42	14	F1140C	–	BGD	obs 19	500	2	2	239.92
11/08/2022 08:57	8	F1550C	HR 8799	TARG	obs 9	500	36	1	4322.63
11/08/2022 10:43	9	F1550C	–	BGD	obs 11	500	36	2	4322.63
11/08/2022 15:28	12	F1550C	HD 218261	REF	obs 16	500	2	9	239.92
11/08/2022 16:27	13	F1550C	–	BGD	obs 18	500	2	2	239.92
11/07/2022 22:06	2	$F2100W$	HR 8799	TARG	obs 10	20	50	4	314.20
11/08/2022 00:50	5	$F2100W$	HD 218261	REF	obs 17	20	05	4	314.20

Notes. Main parameters of the observations: date/time, order of execution in the sequence, filter, name of the object, type of object (target or reference, or background image), identifier of the sequence, number of groups, number of integrations, number of dither positions (9 is for the SGD, 4 or 1 is a classical dither, 2 is for the background), total exposure time per dither.

The reference star, HD 218261, was chosen: 1) to be angularly close to the target (∼1.24°) to minimize the wavefront errors induced by thermal drift and 2) with comparable magnitudes to HR 8799 in both the K band, and the MIRI's coronagraphic filters, so that it can be shared with the NIRCAM GTO program, with the goal to optimize overheads in telescope pointing. Taking into account the stellar residuals and the background noise from our diffraction model (Boccaletti et al. 2015), the exposure times were determined to achieve signal-to-noise ratios (S/Ns) larger than ∼10 on the planets. The total exposure times on target are 1080 s, 1080 s, 4322 s, and 1257 s for the F1065C, F1140C, F1550C, and $F2100W$ filters, respectively.

2.2. Data reduction

We retrieved the processed data from the Mikulski Archive for Space Telescopes (MAST[1]), and also reprocessed the raw data with the latest pipeline version 1.12.5 and jwst CRDS reference files 1140. Here, we outline the main steps of the process. Stage 1 of the JWST pipeline[2] takes as its input the uncalibrated files (`uncal`) and applies the detector-level corrections to raw JWST ramps to produce the 2D slope product. Stage 1 corrects for the dark current and bad pixels such as those that would be saturated or impacted by cosmic rays that would produce jumps in the ramp. Carter et al. (2023) noted that the default jump threshold value is too low and leads to erroneously flagged bad pixels. Therefore, we ran the steps with different values, but we find that it does not have any impact on the calibration. In comparison to ERS data (Hinkley et al. 2022), the ramps in this program have many more groups per integration. Therefore, the jumps have less impact on the calibrated slopes. The first and last group of each integration are removed and the ramps are fitted to generate the `rate` files.

Stage 2 of the JWST pipeline is meant to photometrically calibrate the data. However, because the 4QPM produces a shadow pattern along its transition due to diffraction effects, we skip the `flat_field` steps to avoid increasing the noise as well as the "glow-stick" effect close to the mask center (precisely where we expect to detect the planets). According to the calibration files, skipping this step would introduce an error of about 2% that is much smaller than the final photometric accuracy (see Sect. 3). Stage 2 also subtracts the background and apply the photometric calibration to convert count values to physical units. For MIRI coronagraphic data, photometric calibration is validated and available since version 1.12.5 of the pipeline. `cal` files are expressed in MJy sr^{-1}. Both `rate` and `cal` files collapse all integrations (N_{int}) in a single frame, yielding a number of frames that is the number of dither positions (N_{dither}).

When using `rate` files only, the background is estimated from a mean combination of the background dithers which is subtracted from each target observation. From the image histograms, we identified (both in the `cal` and `rate`+background subtraction) that the background is not perfectly removed. Therefore, we further subtracted a constant value that is estimated from the pixels statistics in two areas of the image (top and bottom left) relatively free of the stellar signal or contamination objects. Finally, bad pixels that are identified as NaN values by the pipeline (in `cal` and `rate` files) are replaced with the mean of the pixels in a 3×3 pixels box. As long as the sigma clipping process is applied to the whole image iteratively, pixels that are not flagged as NaN but deviate from more than 3σ of the mean in the same box are also corrected for. In the following, we describe how we use `rate` files to estimate planet's contrast and `cal` files to directly extract the planet's photometry from the counts.

Each coronagraphic image is registered at the 4QPM center. Similarly to the commissioning (Boccaletti et al. 2022), the center positions were derived by cross-correlating the data with a large database of simulated coronagraphic images. We obtained the following coordinates: [120.25,113.00], [119.77, 113.16], and 119.73, 114.20], for F1065C, F1140C, and F1550C, respectively.

The raw coronagraphic images are essentially dominated by the diffraction. This specific signature (shown at the top of Fig. 1) is the result of the particular JWST hexagonal pupil,

[1] https://mast.stsci.edu/portal/Mashup/Clients/Mast/Portal.html
[2] jwst-pipeline.readthedocs.io

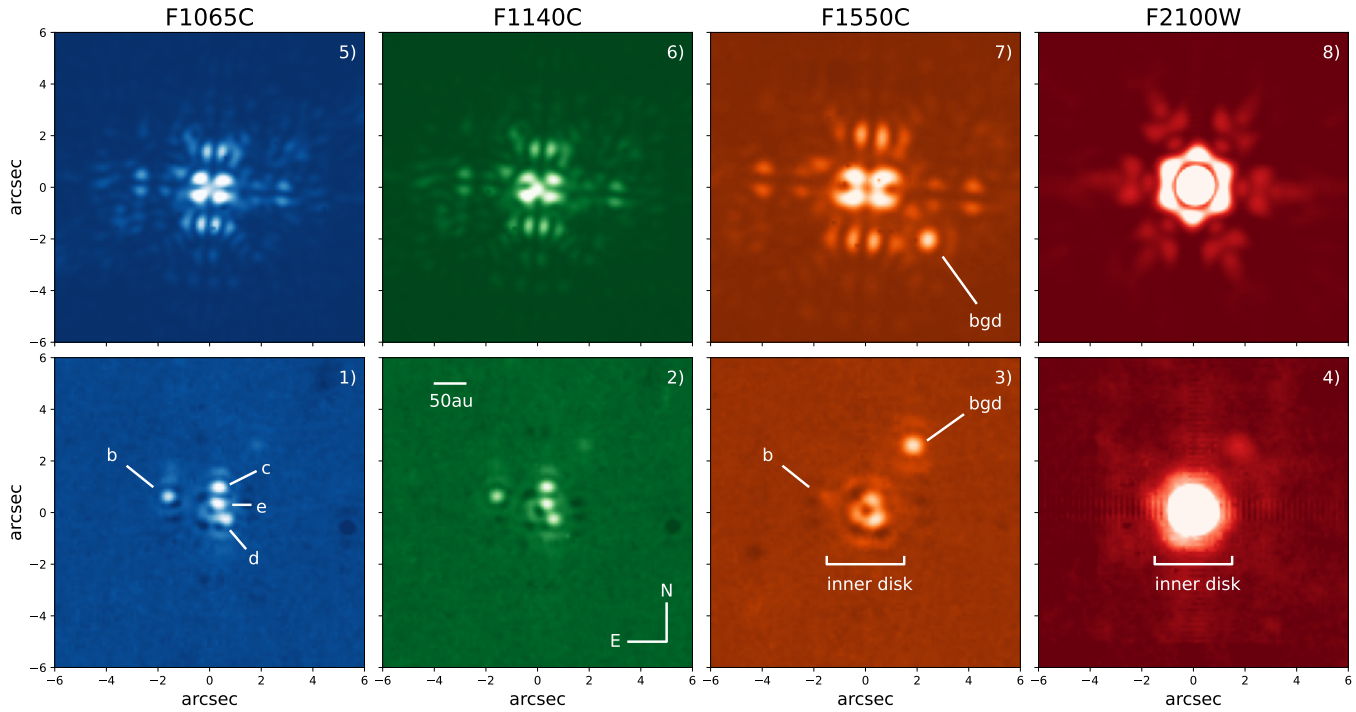

Fig. 1. Raw coronagraphic (top, detector orientation), and reference star subtracted (bottom: north is up, east is left) images in the four filters (left to right: F1065C, F1140C, F1550C, $F2100W$). The four planets are labeled b, c, d, and e in panel 1, as well as the background object in panels 3 and 7. The signature of the inner disk is indicated in panels 3 and 4. The 50 au scale stands for the projected physical distance. The Field of View is $12 \times 12''$. Intensity scale is adapted in each panel for visualisation purpose.

which even an optimized Lyot stop cannot completely suppress (Boccaletti et al. 2005). The classical workaround is to observe a reference star in similar conditions, referred to as reference differential imaging (RDI). However, it has been shown that the contrast achieved with MIRI's 4QPM is mostly limited by the relative pointing accuracy between the target star and the reference star (Cavarroc et al. 2008b), estimated to be about 5–10 mas (Rigby et al. 2023). To mitigate this issue, Soummer et al. (2014) and Lajoie et al. (2016) proposed the small grid dither (SGD) strategy. While we can obtain a single pointing of the target (i.e., with a precision of about 5–10 mas), several (i.e., 5 or 9) pointings of the reference star are performed to provide diversity, as well as to match, ideally, the diffraction pattern of the reference star with that of the star. Elaborate algorithms like `PCA` (Soummer et al. 2012) and `LOCI` (Lafrenière et al. 2007) can provide an optimal subtraction of this diffraction pattern.

For the coronagraphic observations of HR 8799, we used the nine-point SGD, defined as a regular square grid with 10 mas steps. We compared several types of algorithms to suppress the star's diffraction pattern, but since the diversity is low, the best results are obtained with a linear combination of the nine reference frames. Of these, the coefficients are calculated with a downhill simplex method (referred to as `amoeba` in the IDL software library) applied to a restricted annular field of view of 0.4″ to 8″ in radius (Fig. 1, bottom). The combination of the frames, which minimizes the residuals in this field, is then subtracted out from the target image.

The so-called over-subtraction (Pueyo 2016) can be particularly strong in the case of MIRI observations given that the angular separations of the planets are not significantly larger with respect to the angular resolution (about 0.3″ at 10 µm). To overcome this issue, we further masked the planets in the RDI process. In practice, we used a simple aperture of 1 λ/D in radius to remove the contribution of the planet's signal in the minimization of the residuals. In fact, as mentioned above, the central region of the image within 0.4″ is also masked allowing the inner disk to be detected (see Sect. 5). We also tested a method which subtracts the planet's diffraction pattern (taking into account the coronagraph's transmission, see Sect. 3.2), but this requires a first iteration with masks to evaluate the planets' fluxes. Both methods were found to be qualitatively similar although the latter provides larger error bars. Figure 1 displays the results with the masking technique, while other methods including variations of `amoeba`, together with a median combination of the reference frames, and `PCA` with various sets of reference stars, are presented in Fig. A.1 in the appendix.

For the observations in the $F2100W$ filter in standard imaging mode, we used a standard four-point dithering to minimize the impact of the background and cosmetics of the detector. The reference star is observed the same way. Since the inner part of the image (essentially the PSF peak) is dominated by the inner disk flux (see Sect. 5), we performed a direct weighted subtraction to minimize the diffraction in the 2–5″ annular region (to exclude the region where the inner disk dominates).

2.3. Overall description of the images

The four known planets (HR 8799 b, c, d, e) are aptly detected at the two shortest wavelengths (see F1065C in Fig. 1-1 and F1140C in 1-2), while presumably only planet b is detected at F1550C (Fig. 1-3). However, interestingly, planet c is also barely detected at F1550C with the `PCA` reduction technique using the commissioning stars as references (Fig. A.1). The longest wavelength filter ($F2100W$, Fig. 1-4) yields no planet detection. Another point source to the northwest of the star, a suspected background galaxy (Faramaz et al. 2021) labeled "bgd" in

Fig. 1-3 and Fig. 1-7, appears to be very bright at F1550C; it is also visible, but much more faintly, in the other three filters (see Sect. 6). Finally, at the longest wavelengths (F1550C in Fig. 1-3 and $F2100W$ in Fig. 1-4), residual emission at the center of the images corresponds, presumably, to the inner warm debris disk. The same feature is also identified at shorter wavelengths with much lower S/N values. The doughnut-like shape of the inner disk in Fig. 1-3 is due to the coronagraphic effect. It does not capture the actual size of the disk but the extent of its image (see Sect. 5 for details). Overall, the MIRI images of the HR 8799 system yield a very different vision than in the near IR, with the clear detection of the four planets, together with a localized but extended central emission.

3. Photometry of the planets

Extracting the photometry in the MIRI coronagraphic images can be done in two ways: either from contrast measurements or relying on the photometric calibration. The former requires normalization of the planet's flux to the stellar point spread function (PSF) to derive the contrast values, as well as to take into account the planet's attenuation due to the coronagraph and to estimate photometric error bars.

3.1. PSF normalization

To avoid saturation, the star cannot be observed out of the coronagraphic mask. There is no direct way to measure the star-to-planet contrast in the very same filter with this program (or any others) and this is certainly a limitation for accurate photometry. Instead, we considered two solutions for normalizing the stellar flux, both relying on commissioning (COM) data, for which we managed to observe a PSF (out-of-mask image) and a coronagraphic image (on-mask image). The first solution makes use of the target acquisition data (TA) in addition to the COM data. TA comes with any coronagraphic sequence to estimate the centroid of the target in a coronagraph subarray in order to move the star right at the location of the coronagraph. The second solution involves the COM data alone which was designed to accurately measure contrasts for all filters, carefully choosing a star that is not too bright to obtain unsaturated PSFs (Boccaletti et al. 2022).

For TA normalization (Eq. (1)), the method consists of measuring the flux ratio of the TA images between the target, HR 8799 ($I_{\rm TA\_targ}$), and the commissioning star ($I_{\rm TA\_com}$), and to apply this factor to the commissioning PSF ($I_{\rm PSF\_com}$) to generate a pseudo HR 8799 PSF ($I^{\rm TA}_{\rm PSF\_targ}$), as follows :

$$I^{\rm TA}_{\rm PSF\_targ} = I_{\rm PSF\_com} \times \frac{\sum_k A_k.I_{\rm TA\_targ}}{\sum_k A_k.I_{\rm TA\_com}}. \quad (1)$$

Here, A_k is a circular aperture containing k pixels which is set here to a 1″ radius. The two TA images (at two dithered positions) follow the same data reduction procedure as other data. We keep the one that is further out from the 4QPM center to avoid attenuation effects after subtracting them to get rid of the background. In the case of HR 8799 observations, TA data were obtained with the neutral density filter (FND). The FND is intentionally broad (8–18 µm) to mitigate the chromatic effects due to the 4QPM, avoiding bias to the centroid estimation (Cavarroc et al. 2008a). However, normalization issues can arise if the science target has a different spectral slope in the FND spectral range than the commissioning star. This is particularly problematic when IR emission, such as an unresolved (or slightly resolved) disk, adds to the total flux of the central source. At the moment, only the FND has been validated against the TA procedure, but for future programs MIRI will allow TA to be carried out with $F560W$, $F1000W$, and $F1500W$ filters as well.

The second solution is based on the calibration of the coronagraph attenuation on the central star using commissionning data. Here, the normalization factor (Eq. (2)) corresponds to the flux ratio of the coronagraphic images ($I_{\rm CORO\_targ}$, and $I_{\rm CORO\_com}$). Because these images are much more extended than in the former case, here A_k represents an aperture of 5″ in radius to encompass the full coronagraphic diffraction pattern. As an advantage with respect to the former solution, this method uses the same coronagraphic filter. Still, the target and commissioning star are different, and, again, the presence of an unresolved inner disk can bias the normalization. This method is also prone to biasing because of background objects since the aperture, A_k, is much larger to encompass the full coronagraph diffraction pattern. The pseudo-PSF is expressed as:

$$I^{\rm CORO}_{\rm PSF\_targ} = I_{\rm PSF\_com} \times \frac{\sum_k A_k.I_{\rm CORO\_targ}}{\sum_k A_k.I_{\rm CORO\_com}}. \quad (2)$$

Since we have two dithers for $I_{\rm PSF\_com}$ (rejecting two other dithers for image quality reasons), and nine dithers of $I_{\rm CORO\_com}$ (because observations used nine-point SDG) we can evaluate, respectively, 2 and 18 values of the star's count, for $I^{\rm TA}_{\rm PSF\_targ}$, respectively $I^{\rm CORO}_{\rm PSF\_targ}$, contributing to the uncertainties in the planets' photometry. Therefore, the estimate of the dispersion for each method (TA and CORO) is not based on the same amount of independent realizations. However, overall, we estimate that the normalization factors obtained with the two methods are consistent within 5%, 16% and 37% for filters F1065C, F1440C, and F1550C, respectively. The larger discrepancy at F1550C can be explained by the background contamination, which is stronger at longer wavelengths, and can bias the CORO method. The background galaxy, easily identifiable in the raw coronagraphic frame of HR 8799 (Fig. 1-7), is one potential source of bias.

3.2. Coronagraphic transmission

Each planet in the image has a transmission which depends on its position with respect to the 4QPM center and phase transitions and which also scales with wavelength. We estimate this transmission using the diffraction model from Boccaletti et al. (2015) calibrated against commissioning data (Boccaletti et al. 2022), with updates of the telescope wavefront error measurements measured at commissionning. This diffraction model is based on a similar concept as `webbpsf` (Perrin et al. 2014), so that the planet's transmission can be also evaluated with the latter.

We used `whereistheplanet` (Wang et al. 2021) to estimate the planets' locations at the epochs of observations with respect to the 4QPM mask orientation (which is inclined by 4.835° with respect to the detector), accounting for the field orientation (the V3PA parameter in the JWST coordinate system). The estimated values of the coronagraphs' transmission are provided in Table 2 and used to correct for the planets' photometry. To give an idea of the impact of the coronagraph transmission, we display in Fig. B.1 the image of four point sources of equal intensities located at the positions of the HR8799 planets.

Table 2. Coronagraphic transmission.

Planet	F1065C	F1140C	F1550C
b	0.81/0.82	0.75/0.79	0.77/0.82
c	0.78/0.80	0.75/0.78	0.62/0.65
d	0.61/0.67	0.60/0.65	0.62/0.66
e	0.56/0.58	0.52/0.56	0.40/0.45

Notes. The transmission of the 4QPM coronagraphs at the planet location is calculated for a point source in each filters, either in an aperture region of 1.5 λ/D in radius, or integrated in the whole image.

Table 3. Star-to-planet contrasts.

Planet	F1065C	F1140C	F1550C
b	2699 ± 283	2395 ± 363	2388 ± 826
c	1334 ± 324	1252 ± 321	>495
d	1194 ± 345	1181 ± 345	>355
e	945 ± 337	848 ± 271	>234

Notes. Mean and error contrast's values are measured for planets b, c, d, and e, in the three coronagraphic filters.

Table 4. Photometry of the star retrieved from VizieR.

Wavelength (μm)	Flux (W m^{-2})	Flux (Jy)	Flux error (Jy)	Filter
1.24	2.69e-11	11.1	0.3	2MASS:J
1.65	1.47e-11	8.11	0.13	2MASS:H
2.16	7.50e-12	5.41	0.09	2MASS:Ks
3.35	2.29e-12	2.56	0.52	WISE:$W1$
4.60	1.07e-12	1.64	0.12	WISE:$W2$
11.6	6.17e-14	0.238	0.004	WISE:$W3$

3.3. Planets' contrasts and fluxes

The planets' photometry is assessed in two different ways, either by measuring the contrast in `rate` files, or directly measuring the flux density in `cal` files. The photometric extraction also relies on two methods. First, we integrate the planets' count rates (in DN s^{-1}) in RDI images, in an aperture of 1.5 λ/D in radius, the size of which is found to be optimal to integrate enough each planet's signal, while keeping the contamination of the other planets at a low level. Second, we use negative fake planets. As explained in Sect. 3.2, we modeled the planets' diffraction pattern for each filter and each planet positions with respect to the 4QPM transitions. The minimization of the residuals in the 1.5 λ/D area accounts for three parameters: the flux and the positions of the planet's model (which is allowed to vary by a few pixels compared to the theoretical positions). We display in Fig. C.1 the results of the planet's model subtraction for each planet and each filter. The final contrast is the count rates measured in the stellar PSF (Sect. 3.1) relative to the count rates measured on the planet, in the same aperture of 1.5 λ/D, and corrected by the local attenuation due to the coronagraph. With respect to the compensation of the inherent over-subtraction of RDI mentioned in Sect. 2.2, we opted for the method using masks, which offers lower error bars.

Irrespective of the PSF normalization, the two methods to extract planet's photometry can be in good agreement to better than 1% (for instance planet b in F1065C) or it can differ by 50% at most (for instance planet d in F1065C), but are generally consistent within 30–40%. Most of the differences actually come from the type of PSF normalization applied, which in some cases can result in two families of contrast values. Table 3 provides the average contrast values and error bars, while the individual measurements for each PSF normalization and flux extraction methods are given in Table D.1.

Converting contrasts to fluxes requires a stellar flux model. We retrieved synthetic photometry from Virtual Observatory SED Analyzer (VOSA, Bayo et al. 2008), considering the BT NextGen stellar model (Allard et al. 2011; Asplund et al. 2009) with an effective temperature $T_{\rm eff}$ = 7600 K, a surface gravity $\log(g)$ = 4.5 cm s^{-2}, and solar metallicity. We adopted a stellar radius of 1.34 $R_\odot$, and a distance d = 40.88 pc (Gaia Collaboration 2021). Furthermore, we obtained the actual photometry of HR 8799 from VizieR in the 2MASS and WISE filters: J, H, Ks, $W1$, $W2$, and $W3$ (Table 4), excluding the shorter wavelengths (which may not be representative with respect to interpolating the mid-IR fluxes), as well as wavelengths longer than 20 μm to avoid being biased by the emission from the debris disk. We performed a χ^2 minimization to determine the global intensity offset between the model and the real star's photometric data and found a correction of a factor of 1.22. Figure 2 shows the flux density of the four planets as measured in the MIRI filters, with the over-subtraction compensated (and without to see the corresponding impact), together with the near-IR photometry from the literature, which is compiled in Bonnefoy et al. (2016). The flux densities are reported in Table 5 for each planet and each filter.

Proceeding with `cal` files the pixel values are directly provided in MJy steradian^{-1}, with one pixel representing 2.844 × 10^{-13} steradian. We used the same two methods of photometric extraction, aperture, and negative fake planet. Since it is not a relative measurement and the final flux is integrated in a 1.5 λ/D aperture, we need to apply a correction factor to estimate the total fluxes of the planets. This correction is the flux ratio in a planet image (hence, different for each planet, each filter) between 1.5 λ/D and a larger aperture that we set 10 times larger. As reported in Table 5 and Fig. 2, the mean values are found to be compliant with those estimated from the contrast, especially at F1065C and F1140C, but systematically larger at F1550C and $F2100W$ (for planet b and the bgd object).

The reliability of the flux extraction procedure is assessed with a fake planet injection method. To avoid issues of normalization we used `cal` files only. Because the very inner part of the image is very crowded with the planets' diffraction pattern and the inner disk signature, the fake planet is injected at the same angular separation as planet b and the same distance from the 4QPM transitions. The fake planet is generated again from the diffraction model. We choose a flux that is comparable to planet b and account for the attenuation of the coronagraph. In a very simplistic case in which the coronagraphic starlight pattern is artificially cancelled out, we are able to recover the injected flux at a 1–2% precision with both the aperture and negative fake planet extraction method. We estimate that the limitation comes mainly from the ability to model the planet's PSF. In a more realistic case including the starlight pattern and involving the RDI process, the photometric uncertainty is lower than 10% on average with better results using the negative fake planet except at F1550C. Therefore, most of the photometric errors that are found if using the contrast are coming from the assumptions of the normalization factor.

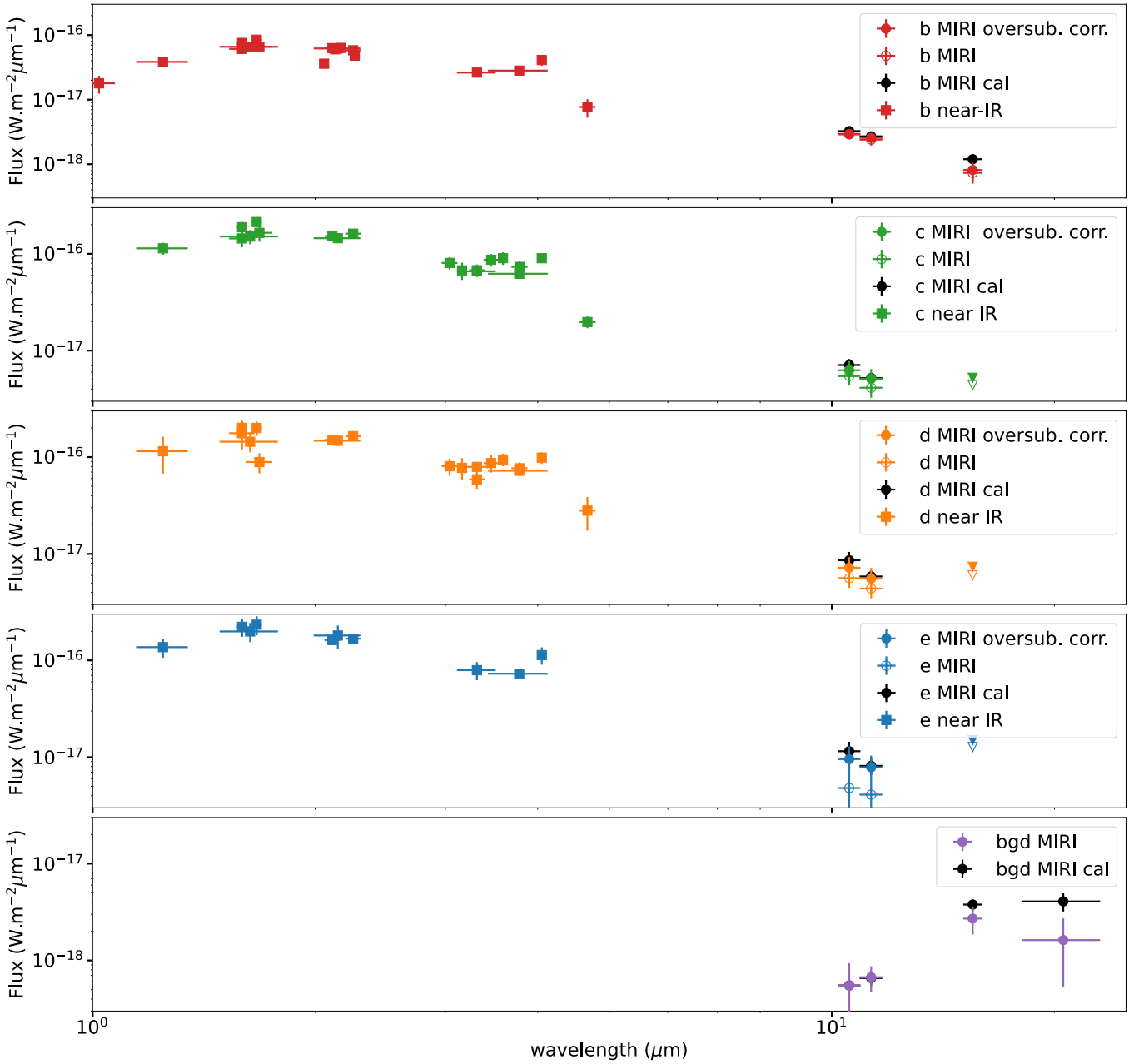

Fig. 2. Flux density in W m^{-2} µm^{-1} of the four planets and the background object in the MIRI filters, with (filled circles) and without (unfilled circles) correcting for the over-subtraction, and in the near IR (squares). The black circles stand for the flux measured in photometrically calibrated data. Triangles denote flux upper limit.

4. Atmospheric modelling

We explored the properties of the planets' atmospheres with two complementary models: `Exo-REM` and `ATMO`, both developed for long period young giant planets, neglecting the stellar irradiation. They both provide grids of synthetic spectra with various atmospheric parameters.

`Exo-REM` (Baudino et al. 2015; Charnay et al. 2018) is a self-consistent 1D radiative-convective equilibrium model which assumes the net flux is conserved. It incorporates the opacities of collision-induced absorptions (H_2–H_2, H_2–He, H_2O–H_2O, and H_2O–N_2), and rovibrational bands from various molecules (H_2O, CH_4, CO, CO_2, NH_3, PH_3, TiO, VO, H_2S, HCN, and FeH), as well as resonant lines from sodium and potassium. `Exo-REM` uses micro-physics to model clouds of silicate, iron, sulfide, alkali salt, and water clouds, and it handles disequilibrium chemistry as well.

`ATMO` (Tremblin et al. 2016, 2017) shares a similar approach for modeling the atmospheres, but it assumes that the thermochemical instability of the CO/CH_4 and N_2/NH_3 transitions can reduce the temperature gradient in exoplanet atmospheres, acting in a similar way as clouds for reddening the spectra, but solving the issue of the J band brightening at the L/T transition (Burrows et al. 2006). This process is controlled by an effective adiabatic index, γ, which is lower than for the thermodynamic equilibrium.

Both models are computed for a range of effective temperature, T_{eff}, surface gravity, log(g), metallicity, and C/O ratio. The details of the grid used in ours analysis are described in

Table 5. Flux densities of the four planets.

Planet	Method	F1065C	F1140C	F1550C
b	rate	2.95 ± 0.31	2.56 ± 0.39	0.81 ± 0.28
	cal	3.26 ± 0.02	2.70 ± 0.04	1.20 ± 0.19
c	rate	6.27 ± 1.52	5.12 ± 1.31	<2.58
	cal	7.10 ± 1.09	5.21 ± 0.66	<1.46
d	rate	7.19 ± 2.08	5.55 ± 1.62	<3.57
	cal	8.59 ± 1.89	5.84 ± 0.97	<6.72
e	rate	9.55 ± 3.41	7.87 ± 2.51	<4.83
	cal	11.52 ± 2.90	8.13 ± 1.59	<9.27

Notes. Fluxes in $\mathrm{W\,m^{-2}\,\mu m^{-1}}$ ($\times 10^{-18}$) for each MIRI filter (mean/error), are provided for the contrast method (`rate`), and the photometrically calibrated files (`cal`).

(Petrus et al. 2023). Since MIRI coronagraphic data only provide photometry, we intentionally compared them to near-IR photometric data from the literature and we reduced the parameter space to two: $T_{\rm eff}$ and $\log(g)$, together with γ in the case of `ATMO`, leaving the metallicity and C/O ratio for further investigations (assuming solar values in this case).

For the sake of simplicity, since the objective of this paper is not a thorough exploration of planet's atmosphere properties, we use here standard χ^2 minimization to determine the best fit to the data. Alternatively, we consider near-IR data alone, or both the near-IR and mid-IR data points. As the mid-IR flux is directly proportional to the product of the effective temperature and the emitting surface of the planet, using only mid-IR photometry would obviously result in a strong degeneracy between temperature and radius. The radius determines the intensity scaling factor between the data and the model and corresponds to the value which nulls the derivative of the χ^2. It is expressed as:

$$R^2 = \frac{\sum_\lambda S(\lambda) \times M(\lambda)/\sigma(\lambda)^2}{\sum_\lambda M(\lambda)^2/\sigma(\lambda)^2} \quad (3)$$

with $S(\lambda)$ as the data (planet's emergent spectrum), $M(\lambda)$ the model, and $\sigma(\lambda)$ the errors, evaluated in the spectral bandpasses of the photometric filters.

We proceeded with both sets of photometric values derived from the contrast measurements (`rate`), and from photometrically calibrated files (`cal`). In the former, the large error bars, due to the dispersion in the normalisation, prevents (in most cases) the model from fitting the mid-IR data points, since the minimization is essentially driven by the near-IR data. To overcome this issue we restrict the number of near-IR data, picking one wavelength value in the standard Y, J, H, K, and L filters. In the latter, we accounted for all near-IR data. The results are displayed in Fig. 3.

Starting with photometrically calibrated values and all near-IR data (top four subpanels in Fig. 3), the two models, `ATMO` and `Exo-REM`, qualitatively reproduce the spectral slope well overall, but yield large reduced χ^2 values indicative of a poor fit in most cases. In general, they systematically predict lower fluxes in the 10–15 µm range than the measured photometric values. Including the mid-IR photometry in the fit together with the near-IR provide much larger reduced χ^2 than near-IR alone, but this is not surprising for such a large spectral range covering more than an order of magnitude.

Planet b is the only case for which adding the mid-IR photometry makes a net difference in the fit compared to using the near-IR photometry alone. However, in this particular case, we suspect that the fit of the near-IR data could be impacted by the photometry in the M band filter (4.67 µm) possibly explaining the low flux beyond 5 µm. The rather low flux in this spectral band measured from the ground (Keck data, Galicher et al. 2011) would call for further investigations, for instance, with JWST/NIRCAM data. The combination of MIRI and near-IR ground-based photometry provides a larger estimate of the planet b radius compared to the literature (based on near-IR data): 1.04 and 1.17 $R_{\rm J}$, for respectively `ATMO` and `Exo-REM`, as opposed to 0.54 and 0.79 $R_{\rm J}$. It appears more compliant with the expectation of evolutionary models (Phillips et al. 2020), although not yet at the predicted value for such an age (~1.3 $R_{\rm J}$). In addition, the temperature of planet b would be cooler, 1000 K and 950 K for `ATMO` and `Exo-REM`, respectively, instead of 1300 K and 1050 K. Interestingly, the F1550C photometric data point is not well aligned with the expected slope of a planet SED (top red subpanel in Fig. 3), contrary to the contrast measurements (bottom red subpanel in Fig. 3), suggesting possibly a calibration error in this filter.

The same tendency (lower temperatures, larger radii) is also observed, but marginally, for the other planets when incorporating mid-IR data in the fit. We hypothesize that a possible reason for this difference in the mid-IR is because the estimation of error bars are not consistent between all the photometric data points in the literature (likely underestimated). There can be calibration issues among instruments, as well or the models might not be fully representative. In the case of HR 8799, the more numerous near-IR measurements naturally drive the models to converge to lower radii and higher temperatures.

For planets b and d, we note that `ATMO` produces very small and possibly unphysical surface gravity which can be as low as $\log(g) = 2.5$, while `Exo-REM` values are more in the higher range, also with possible unphysical values as high as $\log(g) = 5.0$ for planet c. However, trying to derive the surface gravity with a few photometric data points is likely difficult as it mostly affects the depth of spectral features which we are not sensitive to with MIRI coronagraphy. Apart from planet b, the temperatures derived for the other planets are consistent with the values derived by Bonnefoy et al. (2016), in the range of 1150–1300 K.

The experiment which consist in reducing the number of near-IR data points together with using the mid-IR photometry obtained with contrast measurements yields alternative results (bottom four subpanels in Fig. 3). Not only do the best-fit models all aptly reproduce the mid-IR data points, but overall the corresponding radius values are much larger than previously; in particular, for planet c (1.51 $R_{\rm J}$), d (1.37 $R_{\rm J}$), and e (1.49 $R_{\rm J}$) with `ATMO` and (to a lower extent) with `Exo-REM`. We also note that for `ATMO` the derived surface gravities of the four planets are more consistent with expectations ($\log(g)$ = 3.5–4.5) while `Exo-REM` yield overly large values ($\log(g)$ = 4.5–5.0). In the future, with more elaborated atmospheric modeling based on near and mid-IR spectroscopic data to come, it would be interesting to use these radius constraints as inputs. An alternative explanation which is not investigated here is that of an IR excess to account for higher photometric values in the mid-IR. While those planets are likely too old to retain a formation circumplanetary disk, an IR excess could also result from a cloud of dust particles surrounding the planet possibly due to collisions or disruptions of satellites, or even Saturn-like rings, as recently investigated in the case of β Pictoris (Skaf et al. 2023). However, it is beyond the scope of the paper but it is important to underline this important aspect when dealing with mid-IR high contrast imaging.

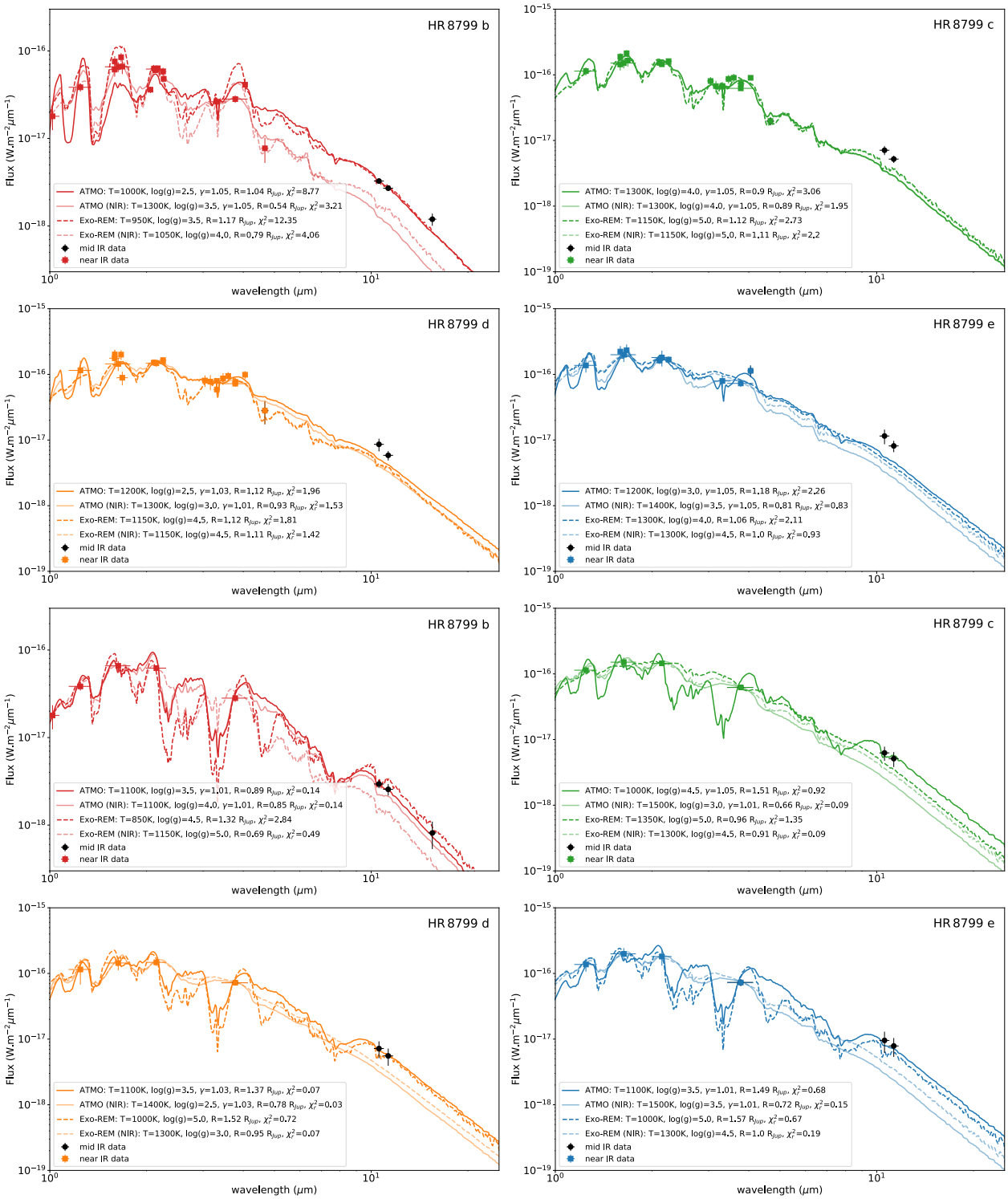

Fig. 3. Flux density in W m^{-2} µm^{-1} of the best models using `ATMO` (plain lines) and `Exo-REM` (dashed lines) fitting the near-IR (colored squares) and mid-IR (black circles) photometric data points for the four planets. The light color lines correspond to the fit of the near-IR data alone. The top four subpanels are for the photometrically calibrated files, and the bottom four are relative to contrast measurements with a reduced number of near-IR data points.

The coronagraphic filters were originally designed to investigate the ammonia feature at ∼10.6 µm (Boccaletti et al. 2015), although the temperatures of the HR 8799 planets are higher than the temperature at which we expect ammonia to clearly stand out in an exoplanet spectrum. Nevertheless, following Danielski et al. (2018) we compare the measured photometry to blackbody spectra in order to distinguish a potential variation of the spectral slope which could be flatter at the shortest coronagraphic filter if ammonia were detectable. In Fig. 4, we plot HR 8799 b photometry (using calibrated photometry) against several blackbody temperatures from 900 K to 1100 K assuming a radius of 1 R_J. Given the error bars, the F1065C and F1140C are the two relevant

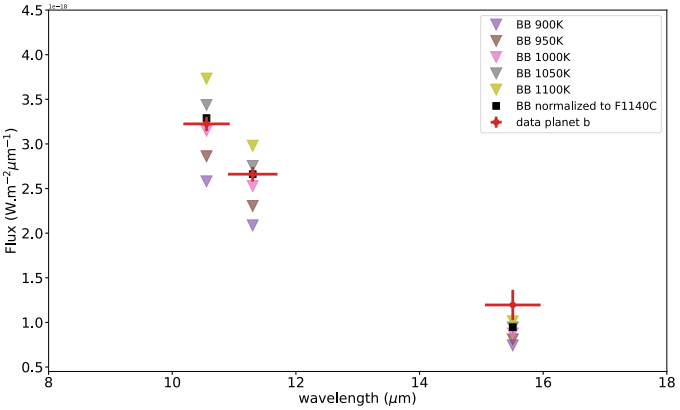

Fig. 4. Flux density (W m^{-2} μm^{-1}) of HR 8799 b (red circles) compared to that of the blackbody for several temperatures (triangles), and if normalized to F1140C (black squares).

filters to derive the equivalent blackbody temperature, which would range from about 1000 K to 1050 K. We may suspect a marginal difference at F1065C between the data and the blackbody, but once the blackbody is normalized to the F1140C data point, the expected blackbody flux at F1065C is fully compatible with the data within error bars. The same applies to the other three planets, which have even larger photometric error bars. As a result, the current data cannot conclude on the detectability of the ammonia feature in the HR 8799 planets.

5. The inner disk component

At F1550C, the central part of the image is dominated by a roughly azimuthally symmetrical pattern in the form of a broad ring surrounded by another thinner ring, which prevents the detection of the innermost planets c, d, and e. The same pattern is also visible, but fainter, in the two other coronagraphic filters, but with a reduced size.

In fact, a warm inner disk component has been identified with Spitzer and is located at physical separations of 6 to 15 au in radius (Su et al. 2009) that is 0.15″ to 0.37″. In principle, the inner disk should be unresolved by MIRI given the angular resolution of about 0.5″ at 15.5 μm. However, such an angular size combined with the extreme sensitivity of the 4QPM coronagraph to pointing, due to its small inner working angle (which is identical to the angular resolution), results in an significant leakage of the inner disk itself (the leakage from the star being much lower in intensity). As a consequence, the inner disk image takes the form of a diffraction pattern, although with a dark spot in the central diffraction peak owing to the strong attenuation of the innermost on-axis beams. Therefore, the rings in the image, which are more extended than the actual inner disk size are reminiscent of a diffraction effect (scaling with wavelengths as proven by the signature at shorter wavelengths), the broad ring and the dark spot being the equivalent of the central PSF diffraction peak, while the thinner ring its first diffraction ring. This is the same effect that hampered the detection of the inner region of the Fomalhaut disk at F1550C, as presented in Gáspár et al. (2023).

Estimating the flux of the inner disk requires modelling the effect of the coronagraph, as a function of the disk size. As already mentioned, this disk component is angularly small and so, it is difficult to constrain its morphology with the present data. Therefore, for the sake of simplicity, we assume a uniform face-on disk model (neglecting the system's orientation), defined by a single parameter, its radius, ranging from 2 to 30 au. We used the diffraction model, as used for modeling a planet's PSF, to generate synthetic disk images. The 2 au case corresponds to a perfectly unresolved case, hence, the image is similar to a raw coronagraphic image of a point source (Fig. 5), but at 5 au, the disk yields a strong leakage, featuring the same kind of pattern that is visible in the real data. Increasing the disk radius does not change the size of its image too much as long as it is fully dominated by diffraction effects. For larger radii (≳30 au), we recovered a more classical image of an extended source, in which the 4QPM transitions generate a shadow pattern on top of the disk image. The top panels in Fig. 5 can be compared with panel 3 in Fig. 1 for further details.

When minimizing the residuals between the real image and the model in a 1.65″ aperture radius (which encompasses the first diffraction ring of the disk), we found an optimal size of 15 au, but 10 au and 20 au also provide a good match. In this case, the 4QPM attenuates the disk by a factor of 7 (5 to 13 for the extreme values), which corresponds to a total flux density of 4.0 ± 0.3 mJy, if we assume the star flux density at 15.5 μm to be 154.2 mJy (interpolating between WISE:W3 and AKARI:L18W). A more realistic, ring-like disk extending from 6 to 15 au, as in Su et al. (2009), yields similar results with a total flux density of 3.1 ± 0.3 mJy; here, the residuals are almost identical to the uniform 15 au case. On the other hand, using the photometrically calibrated files, we measured a flux density of 6.2 mJy, integrated in the same 1.65″ aperture. And, as a sanity check, we obtain a flux density of 152.7 mJy for the star image (the synthetic PSF built from commissionning images), hence in perfect agreement with the aforementioned estimation.

The inner warm disk is also detected at $F2100W$. It is seen as a resolved central emission without any particular structure after subtracting the reference star (Fig. 1-4). There is no coronagraphic attenuation in that case to account for, so the disk flux density can be directly integrated in an aperture of 1.65″. Assuming the star flux density at 21 μm to be 101.8 mJy (interpolating between AKARI:L18W and WISE:W4), we measured a disk flux density of 9.4 mJy. Here, the calibrated files yield a flux density of 31–35 mJy for the inner disk and 332 mJy for the star. While this is consistent in relative flux with the contrast estimation, it is about a factor of 3 larger in terms of absolute flux. This discrepancy is still to be investigated.

To the first order, these values are qualitatively in agreement with the *Spitzer* spectrum presented in Su et al. (2009), but a factor of about 2 lower with respet to the contrast estimations. Su et al. (2009) reported photosphere-subtracted flux densities of ∼8 mJy and ∼19 mJy, at 15.5 μm and 21 μm, respectively. The exact reason behind this discrepancy is still to be investigated, but it could be related either to the reliability of the photosphere subtraction when modeling the spectral energy distribution of the star in the presence of background objects. This may include redshifted galaxies (which can be confused with the star in the Spitzer beam size) up to the limit of our disk model, which does not capture the exact belt geometry, or to the entangling of the disk and planets' images. Finally, the discrepancy in absolute flux for the $F2100W$ filter is to be investigated. Indeed, a larger flux when using `cal` files as opposed to `rate` files is also observed for the background galaxy (see Fig. 2).

Above, we describe how we modeled the inner component as a uniform disk, while the disk image is definitely not symmetrical in brightness at F1550C. We now investigate whether such an asymmetry can be produced by a misalignment of the target onto the coronagraph. Using the diffraction model, we

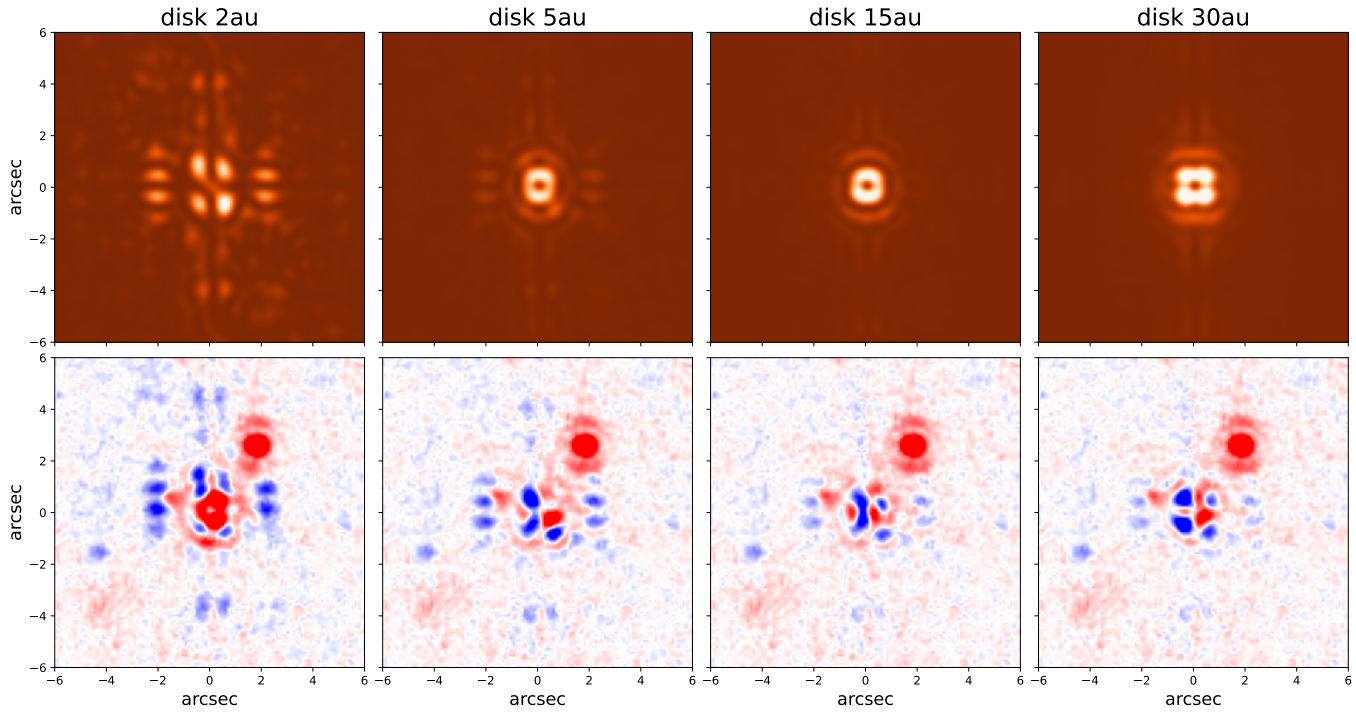

Fig. 5. Coronagraphic images (top) simulated in the F1550C filter for four different disk sizes (2, 5, 15 and 30 au), together with the residuals after subtracting the model to the real F1550C data (reference star subtracted). The intensity scale is adapted in each panel for visualisation purpose. North is up, east is left.

generated uniform disk models of 2 and 15 au in radius that are offset by 0, 50 and 100 mas with respect to the coronagraph. These values are to be compared with the expected pointing accuracy which in principle is typically ten times better. The 2 au size disk model is fully unresolved hence provides a reference coronagraphic image. The results are displayed in Fig. 6. Even if the disk images can be qualitatively comparable to the real data at F1550C for an offset of about 50–100 mas, such an offset would cause the raw coronagraphic images to be very asymmetrical, which is definitely inconsistent with observations. Therefore, we can safely conclude that the brightness asymmetries in the disk image at F1550C are certainly not due to misalignments. Rather, asymmetries would be caused by either the contamination with the planets' PSFs or a variation of the disk density, although the latter is unlkikely given the size of the disk with respect to the angular resolution.

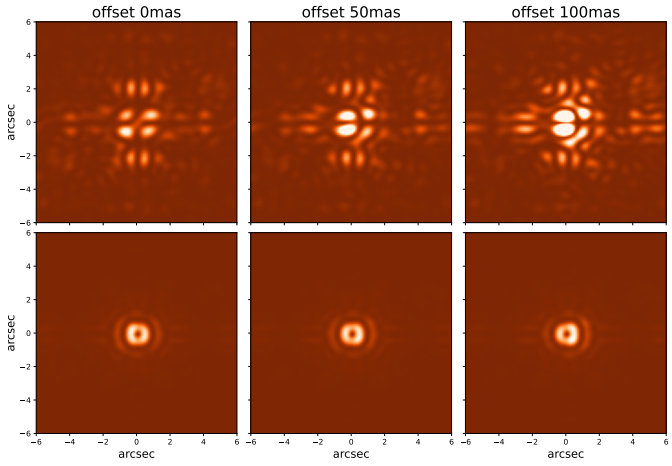

Fig. 6. Coronagraphic images simulated in the F1550C filter for a disk size of 2 au (top) and 15 au (bottom) and for three offset amplitudes (0, 50, and 100 mas). The intensity scale is adapted in each panel for visualisation purpose. In contrary to Fig. 5, the orientation of the 4QPM coronagraph is aligned with the image axis.

6. Background object

Searching for additional planets in the HR 8799 system, either closer in or further out, is motivated by the structure of the debris disk made of two belts. In particular, the inner edge of the outer belt, which (depending on studies) is located at a distance of 110 au (Wilner et al. 2018) or 145 au (Booth et al. 2016) could be caused by a fifth sub-Jupiter to Saturn mass planet (Read et al. 2018).

In this respect, the F1550C image reveals a bright point source located at $\Delta\alpha = -1.653 \pm 0.012''$ and $\Delta\delta = 2.503 \pm 0.020''$ from the star (error bars being conservative since we only have two measurements), which also has fainter counterparts in the other filters. Its photometry in the four MIRI bands is shown in Fig. 2. With a flux density increasing from 10 µm to 15 µm, it could have been the signature of an object with a low temperature – possibly a planet. However, for the flux to match the expected emission of a planet cooler than the other planets in the system (400 K for instance) it would require a radius much larger than that of Jupiter which is odd given the mass and temperature of the other planets.

An alternative to the planet hypothesis is provided in Faramaz et al. (2021), who identified a point-like source in ALMA band 7 data from 2018, near the inner edge of the outer belt ($\Delta\alpha = -1.28 \pm 0.05''$ and $\Delta\delta = 2.34 \pm 0.05''$), with flux densities of 316 µJy and 58 µJy at, respectively, the 0.87 mm (band 7) and 1.3 mm (band 6). They also showed that the spectral index is too steep to match the expected behavior of a dust clump.

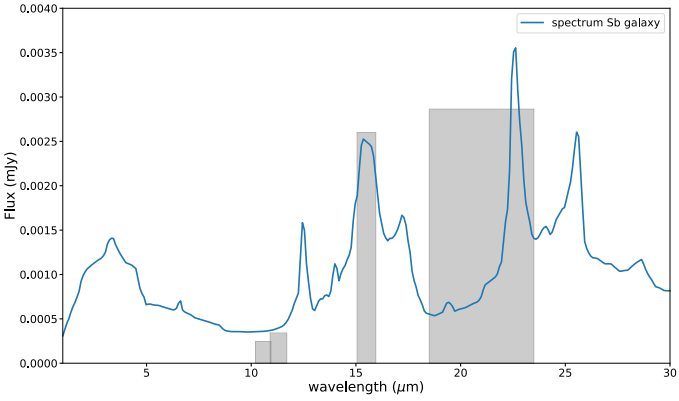

Fig. 7. Typical spectrum of a Sb galaxy at a redshift $z = 1$, taken from the SWIRE template library (Polletta et al. 2007); the relative intensities (corresponding to the photometry measured in Fig. 2) of the four MIRI filters are indicated. A clear excess at 15.5 μm can be observed that could explain the observed fluxes.

As for the astrometric analysis, with respect to the ALMA 2015 data (band 6) in which the same source is marginally detected, the beam size of ALMA does not allow a firm conclusion regarding the motion of the source. Interestingly, the source in the ALMA deconvolved image also seems to be marginally resolved. Faramaz et al. (2021) concluded that the bright source is likely to be a background galaxy.

With a new data point, 4.44 yr apart from the former detection, we can now safely conclude that this is a background object, as the motion between the two epochs is $\Delta\alpha = -0.373 \pm 0.051''$ and $\Delta\delta = 0.163 \pm 0.054''$. This is consistent within $\sim 2\sigma$ with what is expected from the star's proper motion: $\Delta\alpha = -0.48''$ and $\Delta\delta = 0.22''$. As a consequence, given that the radial separation increases from $2.67''$ to $3''$, it is not consistent with an orbital motion for a nearly face-on system.

Furthermore, the characteristics of the spectral energy distribution displayed in Fig. 2, which is peaking at 15 μm, is in line with the 7.7 μm PAH emission of a Sb spiral galaxy redshifted at $z \approx 1$. As a qualitative illustration, Fig. 7 displays a typical spectrum of a Sb galaxy taken from the SWIRE template library (Polletta et al. 2007). In addition, if we compare the relative fluxes of the object in ALMA bands 6 and 7 with the predictions by the redshifted Sb galaxy spectrum, normalized at 10.65 μm, they are fully consistent (ratio 1.0 and 1.12 respectively). In future observations with MIRI's coronagraph, we should expect contamination from background galaxies to complicate the analysis.

7. Conclusions

We summarize the results of the first GTO study with the MIRI coronagraphic mode below:

- We obtained mid-IR observations from 10 to 20 μm of the multiplanet system HR 8799, in both coronagraphy and standard imaging with JWST/MIRI. Once the diffraction and background emission are subtracted out we can easily detect the four planets, including the closest one in filters F1065C and F1140C. Indeed, planet e is found to be lying at the inner working angle and is attenuated by a factor of ∼2 at filter F1140C. This demonstrates the ability of the MIRI coronagraph to probe the very inner regions of exoplanetary systems;
- We developed a procedure to extract and calibrate the photometry of the planets making use of target acquisition data and commissioning data. We identified the oversubtraction as a potential source of error and mitigate this effect by masking the planets in the optimization of the reference star subtraction. Comparing with models of exoplanet atmospheres, we show that MIRI photometry favors larger radii and cooler temperatures, as compared to using near-IR photometry alone. This is particularly true for planet b (1.04 or 1.17 R_J and 950 or 1000 K), but remains marginal for the other planets. Overall, MIRI photometric values are systematically brighter than the models which could indicate a natural difficulty to compile photometries from various instruments, or a missing ingredient in the models. However, reducing the number of near-IR data points to give more weights to mid-IR, yields even larger planets' radii, as large as $\sim 1.5\,R_J$. Taking advantage of NIRCAM to get overlapping data at near-IR, as for HIP 65426 b (Carter et al. 2023), can definitely help to cross calibrate near and mid-IR data. A deeper exploration of the atmospheric properties, based on advanced modeling that takes into account these new MIRI's photometric data, would definitely be relevant;
- In terms of performance, we tested the ability to use a library of reference stars. Even if we managed to obtain reasonable contrasts, the best quality by far is achieved with a dedicated observation of a reference star obtained close in time. This situation will certainly change along the lifetime of JWST, as more targets are observed with MIRI's coronagraphs, providing sufficient observing time is allocated to this mode;
- In line with the capacity of the MIRI's coronagraph at short angular separations, we also directly detect and spatially resolve for the first time the inner warm debris disk in all four filters. By taking into account the diffractive effect of the 4QPM coronagraph we were able to constrain the inner disk radius to about 15 ± 5 au using the F1550C image, which provides a direct and independent estimate in agreement with the modeling of the IR excess. We measured a flux density at F1550C and $F2100W$ of a few mJy, a factor of 2 lower than Spitzer which remains to be understood. The outer cold debris disk is undetected, consistent with the sensitivity;
- In the field of view, we identified a point source which we confirmed to be a background redshifted galaxy at $z \approx 1$ considering the astrometry with respect to ALMA observations, and its spectral energy distribution;
- Finally, the extreme sensitivity of the 4QPM coronagraph at small angular separations combined with the presence of inner circumstellar components can make the detection and the interpretation of young system observations very challenging, particularly with respect to the confusion related to background galaxies. The MIRI's coronagraphic mode is still in its infancy and there is room for improving several aspects: modeling and calibrating the diffraction pattern as a function of telescope characteristics, developing optimal data reduction techniques, and interpreting the entangled signals of point-like sources and extended circumstellar components.

Acknowledgements. This work is based on observations made with the NASA/ESA/CSA *James Webb* Space Telescope. The data were obtained from the Mikulski Archive for Space Telescopes at the Space Telescope Science Institute, which is operated by the Association of Universities for Research in Astronomy, Inc., under NASA contract NAS 5-03127 for JWST. These observations are associated with program #1194. Part of this work was carried out at the Jet Propulsion Laboratory, California Institute of Technology, under contrast with NASA (80NM0018D0004). French contributors acknowledge the support and funding of CNES. This publication makes use of VOSA, developed under the Spanish Virtual Observatory (https://svo.cab.inta-csic.es)

project funded by MCIN/AEI/10.13039/501100011033/ through grant PID2020-112949GB-I00. VOSA has been partially updated by using funding from the European Union's Horizon 2020 Research and Innovation Programme, under Grant Agreement no. 776403 (EXOPLANETS-A) This work has made use of data from the European Space Agency (ESA) mission *Gaia* (https://www.cosmos.esa.int/gaia), processed by the *Gaia* Data Processing and Analysis Consortium (DPAC, https://www.cosmos.esa.int/web/gaia/dpac/consortium). Funding for the DPAC has been provided by national institutions, in particular the institutions participating in the *Gaia* Multilateral Agreement. This research has made use of the VizieR catalogue access tool, CDS, Strasbourg, France (DOI: 10.26093/cds/vizier). The original description of the VizieR service was published in 2000, A&AS 143, 23.

References

Allard, F., Homeier, D., & Freytag, B. 2011, in Astronomical Society of the Pacific Conference Series, 448, 91
Asplund, M., Grevesse, N., Sauval, A. J., & Scott, P. 2009, ARA&A, 47, 481
Barman, T. S., Macintosh, B., Konopacky, Q. M., & Marois, C. 2011, ApJ, 733, 65
Barman, T. S., Konopacky, Q. M., Macintosh, B., & Marois, C. 2015, ApJ, 804, 61
Baudino, J. L., Bézard, B., Boccaletti, A., et al. 2015, A&A, 582, A83
Bayo, A., Rodrigo, C., Barrado Y Navascués, D., et al. 2008, A&A, 492, 277
Boccaletti, A., Baudoz, P., Baudrand, J., Reess, J. M., & Rouan, D. 2005, Adv. Space Res., 36, 1099
Boccaletti, A., Lagage, P.-O., Baudoz, P., et al. 2015, PASP, 127, 633
Boccaletti, A., Cossou, C., Baudoz, P., et al. 2022, A&A, 667, A165
Bonnefoy, M., Zurlo, A., Baudino, J. L., et al. 2016, A&A, 587, A58
Booth, M., Jordán, A., Casassus, S., et al. 2016, MNRAS, 460, L10
Burrows, A., Sudarsky, D., & Hubeny, I. 2006, ApJ, 640, 1063
Carter, A. L., Hinkley, S., Kammerer, J., et al. 2023, ApJ, 951, L20
Cavarroc, C., Amiaux, J., Baudoz, P., et al. 2008a, SPIE Conf. Ser., 7010, 70100W
Cavarroc, C., Boccaletti, A., Baudoz, P., Amiaux, J., & Regan, M. 2008b, PASP, 120, 1016
Charnay, B., Bézard, B., Baudino, J. L., et al. 2018, ApJ, 854, 0
Chauvin, G., Desidera, S., Lagrange, A. M., et al. 2017, A&A, 605, A9
Chen, C. H., Sargent, B. A., Bohac, C., et al. 2006, ApJS, 166, 351
Currie, T., Burrows, A., Itoh, Y., et al. 2011, ApJ, 729, 128
Danielski, C., Baudino, J.-L., Lagage, P.-O., et al. 2018, AJ, 156, 276
Faramaz, V., Marino, S., Booth, M., et al. 2021, AJ, 161, 271
Gaia Collaboration (Brown, A. G. A., et al.) 2021, A&A, 649, A1
Galicher, R., Marois, C., Macintosh, B., Barman, T., & Konopacky, Q. 2011, ApJ, 739, L41
Gardner, J. P., Mather, J. C., Abbott, R., et al. 2023, PASP, 135, 068001
Gáspár, A., Wolff, S. G., Rieke, G. H., et al. 2023, Nat. Astron., 7, 790
GRAVITY Collaboration (Lacour, S., et al.) 2019, A&A, 623, L11
Hinkley, S., Carter, A. L., Ray, S., et al. 2022, PASP, 134, 095003
Hughes, A. M., Wilner, D. J., Andrews, S. M., et al. 2011, ApJ, 740, 38
Ingraham, P., Marley, M. S., Saumon, D., et al. 2014, ApJ, 794, L15
Konopacky, Q. M., Barman, T. S., Macintosh, B. A., & Marois, C. 2013, Science, 339, 1398
Lafrenière, D., Marois, C., Doyon, R., Nadeau, D., & Artigau, 2007, ApJ, 660, 770
Lagrange, A.-M., Philipot, F., Rubini, P., et al. 2023, A&A, 677, A71
Lajoie, C.-P., Soummer, R., Pueyo, L., et al. 2016, SPIE Conf. Ser., 9904, 99045K
Marois, C., Macintosh, B., Barman, T., et al. 2008, Science, 322, 1348
Marois, C., Zuckerman, B., Konopacky, Q. M., Macintosh, B., & Barman, T. 2010, Nature, 468, 1080
Miles, B. E., Biller, B. A., Patapis, P., et al. 2023, ApJ, 946, L6
Mollière, P., Stolker, T., Lacour, S., et al. 2020, A&A, 640, A131
Nielsen, E. L., De Rosa, R. J., Macintosh, B., et al. 2019, AJ, 158, 13
Öberg, K. I., Murray-Clay, R., & Bergin, E. A. 2011, ApJ, 743, L16
Perrin, M. D., Sivaramakrishnan, A., Lajoie, C.-P., et al. 2014, in Proc. SPIE, 9143, 91433X
Petit Dit De La Roche, D. J. M., Hoeijmakers, H. J., & Snellen, I. A. G. 2018, A&A, 616, A146
Petit Dit De La Roche, D. J. M., van den Ancker, M. E., Kissler-Patig, M., Ivanov, V. D., & Fedele, D. 2020, MNRAS, 491, 1795
Petrus, S., Chauvin, G., Bonnefoy, M., et al. 2023, A&A, 670, A9
Phillips, M. W., Tremblin, P., Baraffe, I., et al. 2020, A&A, 637, A38
Polletta, M., Tajer, M., Maraschi, L., et al. 2007, ApJ, 663, 81
Pueyo, L. 2016, ApJ, 824, 117
Read, M. J., Wyatt, M. C., Marino, S., & Kennedy, G. M. 2018, MNRAS, 475, 4953
Rigby, J., Perrin, M., McElwain, M., et al. 2023, Astronomical Society of the Pacific, 135, 048001
Ruffio, J.-B., Konopacky, Q. M., Barman, T., et al. 2021, AJ, 162, 290
Skaf, N., Boccaletti, A., Pantin, E., et al. 2023, A&A, 675, A35
Skemer, A. J., Marley, M. S., Hinz, P. M., et al. 2014, ApJ, 792, 17
Soummer, R., Pueyo, L., & Larkin, J. 2012, ApJ, 755, L28
Soummer, R., Lajoie, C.-P., Pueyo, L., et al. 2014, SPIE Conf. Ser., 9143, 91433V
Su, K. Y. L., Rieke, G. H., Stapelfeldt, K. R., et al. 2009, ApJ, 705, 314
Thompson, W., Marois, C., Do Ó, C. R., et al. 2023, AJ, 165, 29
Tremblin, P., Amundsen, D. S., Chabrier, G., et al. 2016, ApJ, 817, L19
Tremblin, P., Chabrier, G., Baraffe, I., et al. 2017, ApJ, 850, 46
Vigan, A., Fontanive, C., Meyer, M., et al. 2020, A&A, 651, A72
Wagner, K., Boehle, A., Pathak, P., et al. 2021, Nat. Commun., 12, 922
Wang, J. J., Kulikauskas, M., & Blunt, S. 2021, Astrophysics Source Code Library, [record ascl:2101.003]
Wang, J. J., Gao, P., Chilcote, J., et al. 2022, AJ, 164, 143
Wilner, D. J., MacGregor, M. A., Andrews, S. M., et al. 2018, ApJ, 855, 56
Wright, G. S., Wright, D., Goodson, G. B., et al. 2015, PASP, 127, 595

[1] LESIA, Observatoire de Paris, Université PSL, CNRS, Sorbonne Université, Univ. Paris Diderot, Sorbonne Paris Cité, 5 place Jules Janssen, 92195 Meudon, France
e-mail: anthony.boccaletti@obspm.fr
[2] Université Paris-Saclay, Université Paris Cité, CEA, CNRS, AIM, 91191 Gif-sur-Yvette, France
[3] Max-Planck-Institut für Astronomie (MPIA), Königstuhl 17, 69117 Heidelberg, Germany
[4] Institute for Astronomy, University of Edinburgh, Royal Observatory, Blackford Hill, Edinburgh EH9 3HJ, UK
[5] Department of Astrophysics/IMAPP, Radboud University, PO Box 9010, 6500 GL Nijmegen, The Netherlands
[6] HFML – FELIX. Radboud University PO box 9010, 6500 GL Nijmegen, The Netherlands
[7] SRON Netherlands Institute for Space Research, Niels Bohrweg 4, 2333 CA Leiden, The Netherlands
[8] Department of Astrophysics, University of Vienna, Türkenschanzstrasse 17, 1180 Vienna, Austria
[9] ETH Zürich, Institute for Particle Physics and Astrophysics, Wolfgang-Pauli-Strasse 27, 8093 Zürich, Switzerland
[10] Institute of Astronomy, KU Leuven, Celestijnenlaan 200D, 3001 Leuven, Belgium
[11] STAR Institute, Université de Liège, Allée du Six Août 19c, 4000 Liège, Belgium
[12] Université Paris-Saclay, CEA, Département d'Électronique des Détecteurs et d'Informatique pour la Physique, 91191 Gif-sur-Yvette, France
[13] LERMA, Observatoire de Paris, Université PSL, Sorbonne Université, CNRS, Paris, France
[14] UK Astronomy Technology Centre, Royal Observatory, Blackford Hill, Edinburgh EH9 3HJ, UK
[15] Kapteyn Institute of Astronomy, University of Groningen, Landleven 12, 9747 AD Groningen, The Netherlands
[16] European Space Agency, Space Telescope Science Institute, Baltimore, MD, USA
[17] Department of Astronomy, Stockholm University, AlbaNova University Center, 10691 Stockholm, Sweden
[18] School of Physics & Astronomy, Space Research Centre, Space Park Leicester, University of Leicester, 92 Corporation Road, Leicester LE4 5SP, UK
[19] Centro de Astrobiología (CAB), CSIC-INTA, ESAC Campus, Camino Bajo del Castillo s/n, 28692 Villanueva de la Cañada, Madrid, Spain
[20] Leiden Observatory, Leiden University, PO Box 9513, 2300 RA Leiden, The Netherlands
[21] Department of Astronomy, Oskar Klein Centre, Stockholm University, 106 91 Stockholm, Sweden
[22] School of Cosmic Physics, Dublin Institute for Advanced Studies, 31 Fitzwilliam Place, Dublin D02 XF86, Ireland
[23] Jet Propulsion Laboratory, California Institute of Technology, Pasadena, CA, USA

Appendix A: Other data reductions

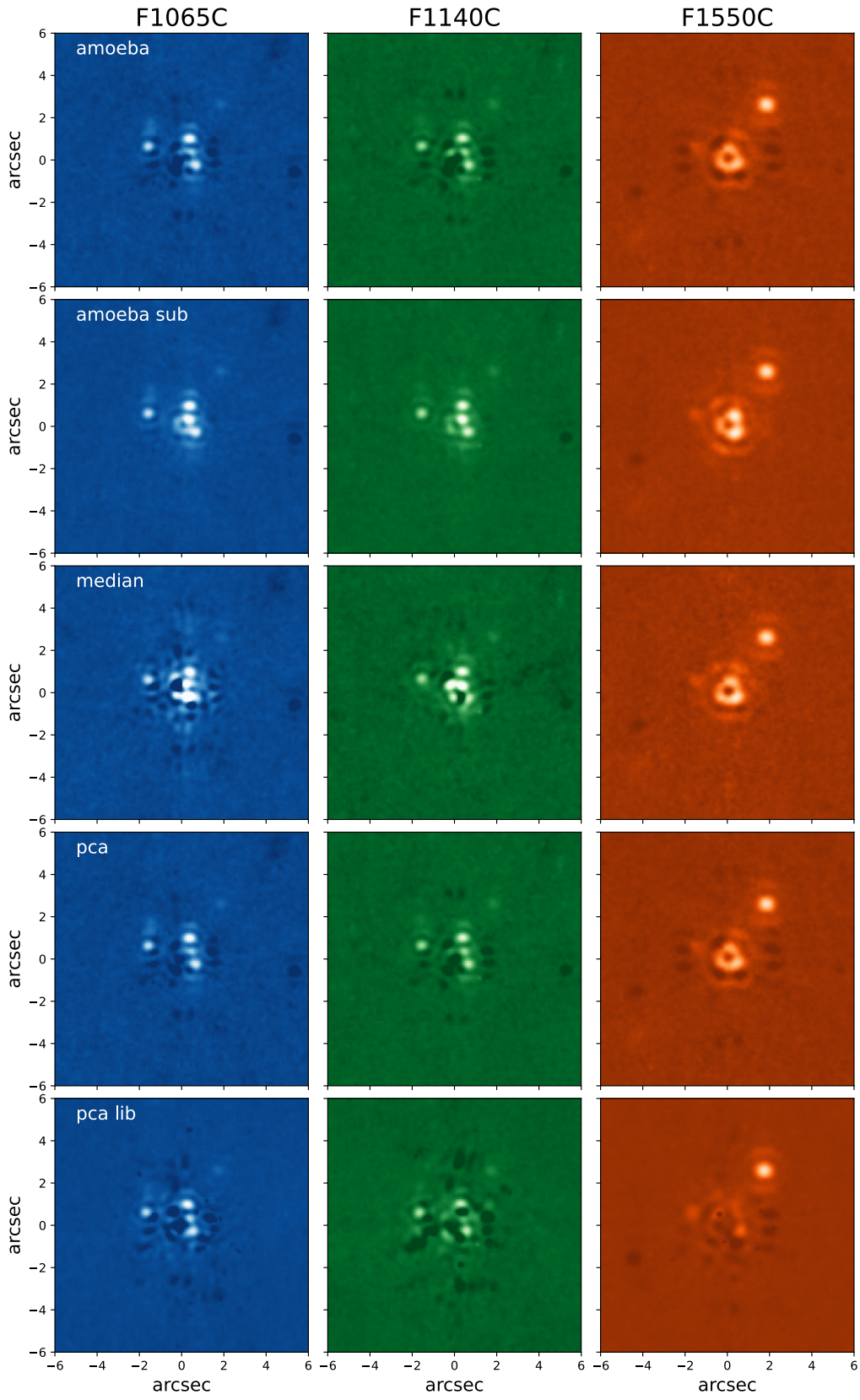

Fig. A.1. Reference star subtracted images in the three coronagraphic filters (left to right: F1065C, F1140C, F1550C) for a variety of algorithms: amoeba (same as in Fig. 1 without masking the planets), amoeba sub. (same as in Fig. 1 with subtracting the planets' diffraction models, median (median combination of the 9 small grid dithers), PCA (principal component analysis of the 9 small grid dithers), and PCA lib (principal component analysis using two other reference stars observed at commissioning, hence totalling 18 small grid dithers). The field of view is 12×12". The intensity scale is adapted in each panel for visualisation purposes.

Appendix B: Planets' footprints

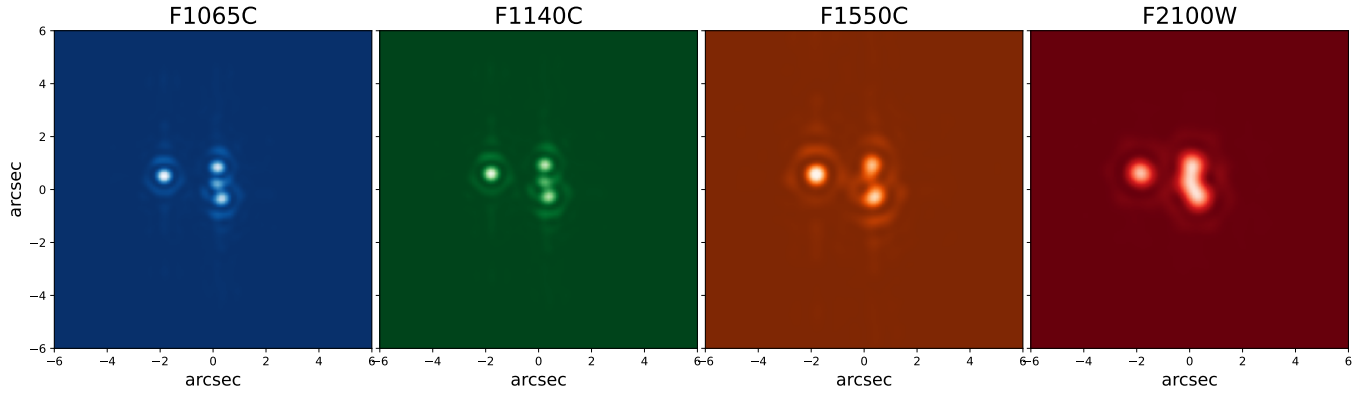

Fig. B.1. Images in each filters of four point sources with equal brightness, but located at the positions of the HR8799 planets to illustrate the impact of the coronagraph transmission as well as the overlapping of the PSFs arising from the angular resolution at such angular separations.

Appendix C: Planets' subtraction

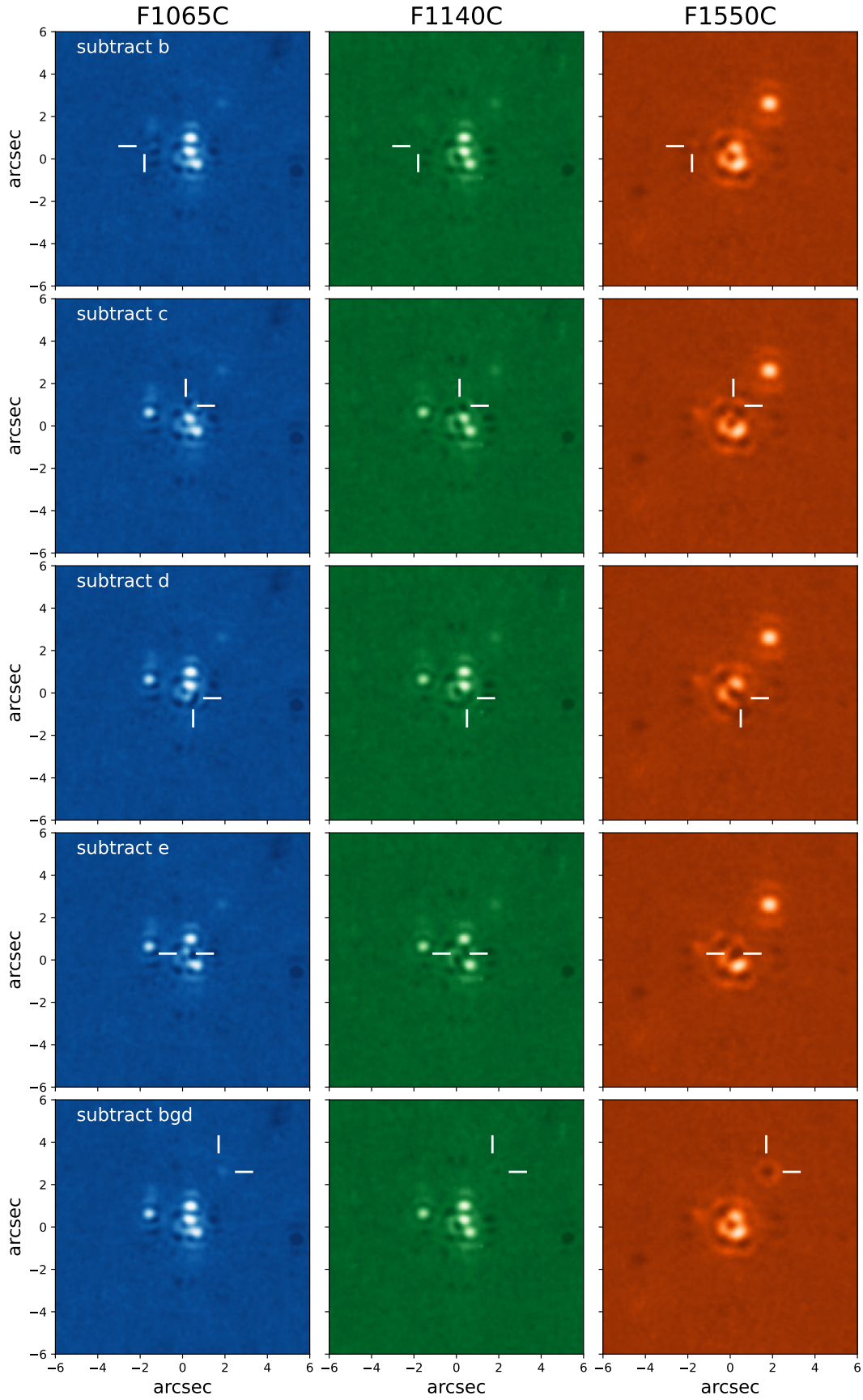

Fig. C.1. Images in each filters of the result of the negative fake planet subtraction for each point source component in the image: the four planets and the background galaxy.

Appendix D: Measured contrasts

Table D.1. Same as Table 3 for each normalization/extraction method.

Planet	Norm. & extrac. method	F1065C	F1140C	F1550C
b	CORO/aper	2757 ± 293	2485 ± 222	2067 ± 221
	CORO/FP neg	2717 ± 288	2417 ± 215	2871 ± 307
	TA/aper	2371 ± 27	1917 ± 23	1391 ± 26
	TA/FP neg	2337 ± 27	1864 ± 23	1932 ± 36
c	CORO/aper	1150 ± 122	1117 ± 100	> 432
	CORO/FP neg	1556 ± 165	1445 ± 128	> 592
	TA/aper	989 ± 11	862 ± 11	> 291
	TA/FP neg	1338 ± 15	1114 ± 14	> 398
d	CORO/aper	971 ± 103	1008 ± 89	> 307
	CORO/FP neg	1450 ± 154	1410 ± 126	> 428
	TA/aper	835 ± 10	777 ± 9	> 207
	TA/FP neg	1247 ± 14	1088 ± 13	> 288
e	CORO/aper	701 ± 74	698 ± 62	> 157
	CORO/FP neg	1215 ± 129	1038 ± 93	> 327
	TA/aper	603 ± 7	539 ± 7	> 106
	TA/FP neg	1045 ± 12	801 ± 10	> 220